CrossMark

# Progressive failure mechanism of a large bedding slope with a strain-softening interface

Q. J. Hu[1] · R. D. Shi[1] · L. N. Zheng[2] · Q. J. Cai[3] · L. Q. Du[1] · L. P. He[1]

**Abstract** The present work is primarily concerned with the progressive failure mechanism of a large bedding slope with a strain-softening interface. Both the laboratory tests and finite difference method (FLAC software) are employed to fulfill our purpose. Firstly, the shear properties of the interface (the mudded weak interlayer) are investigated through groups of repeated shear tests. According to the test results, all kinds of the interfaces share the characteristics of strain softening. To simulate the shear behavior of the interface in FLAC, a contact constitutive model with strain softening is built and verified against experimental results. The modified constitutive model of the interface is later applied to the numerical simulation of the bedding slope. Through investigating the response of the strain-softening contact elements to the stress characteristics among the rock layers, the chain action law of the bedding slope stability can be obtained. Finally, the progressive failure mechanism of the bedding slope is determined based on the chain action law. A typical case is investigated to validate the feasibility of the strain-softening contact element and the progressive failure mechanism of bedding slopes.

✉ L. N. Zheng
zhenglliningzjdx@yahoo.com

1  School of Civil Engineering and Architecture, Southwest Petroleum University, Chengdu 610500, People's Republic of China

2  China Construction Underground Space Co., Ltd., Chengdu 610081, People's Republic of China

3  School of Transportation and Logistics, Southwest Jiaotong University, Chengdu 610031, People's Republic of China

## Introduction

The bedding slope is considered to be one of the most dangerous side slopes because its weak interfaces with poor mechanical properties pose a threat to landslides (Roy and Mandal 2009; Tang et al. 2015; Zhou and Lu 2009). To provide a significant basis for its reinforcement, studies on the failure modes of bedding slopes have been a focus of extensive concern. Specifically, for a large bedding slope with a low inclination angle ($<35°$), the failure mode is not the same as the common type. According to field and literature investigations, bedding slopes present progressive features because their weak interfaces exhibit strain softening during shear processes (Guo and Qi 2015; Lee et al. 2007; Scholtès and Donzé 2015) In view of the great danger of bedding slopes with strain-softening interfaces, a viable method to investigate the progressive failure mechanism seems essential.

The study of the progressive failure of bedding slopes has aroused the greatest attention in recent decades (Białas and Mróz 2005). Various methods have been developed to analyze the stability and failure modes of bedding slopes. Without the claim of being exhaustive, two of the most common methods are presented in the following review.

The first approach to researching the progressive failure is a theoretical study of strain softening. Toshikazu (1981) first simplified the strain softening curve to a tri-liner stress–strain model according to rock triaxial tests, laying the foundation of strain-softening theory. Employing a technique of non-vertical slices, Khan et al. (2002) proposed a limit equilibrium method to analyze the stability of progressive slopes. Furthermore, an analysis of field cases indicates that this method can obtain a reasonable solution in certain conditions where the vertical slice method does not work well. Based on the traditional slice method, Zhang and Zhang (2007) proposed a simplified strain

Springer

compatibility equation that can be used to evaluate the stability of strain-softening slopes. According to the analysis of a homogeneous slope, they determined that the stability of the strain-softening slope is tightly related not only to the strength parameters but also to the stress–strain relationship of the soil. Chai et al. (2007) proposed a relatively simple constitutive model to simulate the strain-softening behavior of soil based on the modified Cam clay model, and the validity of the proposed model was verified by comparing the simulated results with test data. Applying the strength reduction method and termination criterion to the progressive failure analysis of slopes, Zhang et al. (2013) studied the effects with different values of the residual plastic shear strain, elastic modulus, Poisson's ratio and dilation angle.

Compared to theoretical studies, numerical methods in combination with laboratory tests seem to be more popular in the study of progressive failure. Eberhardt et al. (2004) investigated progressive failure in natural rock slopes through a hybrid method that combines both continuum and discontinuum techniques. Focusing on the Randa rockslide, the evolution of failure in massive natural rock slopes as a function of the slide plane development and internal strength degradation was demonstrated (Eberhardt et al. 2004). Troncone (2005) showed that progressive failure would occur owing to deep excavation at the toe of the slope in strain-softening soil by the finite element method. During the process of the simulation, the non-local elasto-viscoplastic constitutive model, which was realized in conjunction with the Mohr–Coulomb model by reducing the strength parameters, was proposed to represent the shear behavior of strain-softening soils. Based on the pragmatic strain-softening constitutive model, Chai and Carter (2009) simulated the progressive failure of an embankment and investigated the effects of strain softening on the response of the foundation soil and embankment behavior by finite element analysis. Using the same method, Conte et al. (2010) assessed the stability of slopes in soils with strain softening. The strain-softening behavior of the soils was simulated by means of reducing the strength parameters and increasing the deviatoric plastic strain (Conte et al. 2010). Using the large deformation finite element analysis based on the updated Lagrangian formula, Mohammadi and Taiebat (2013) evaluated the post-failure deformation of slopes in strain-softening materials. In their study, an extended Mohr–Coulomb constitutive model was employed to simulate the strain-softening behavior of the materials. According to their analysis results, the post-failure deformation was closely related to the strength reduction and the stiffness of the slope materials, both of which had an influence on the initiation of progressive failure in slopes. Using a user-defined Fish program in the finite difference method

FLAC, Wu et al. (2011) developed a non-linear constitutive model to simulate the strain-softening behavior of the interfaces and verified it by comparing the numerical direct shear test with theoretical calculations.

Although existing studies have obtained some meaningful results for the slope stability and failure modes, none of them have systematically investigated the progressive failure mechanism of a large bedding slope with low rock stratum angles. Additionally, to the best of the authors' knowledge, there is little information in the literature about the distribution of bedding planes and joint surfaces among the rock strata.

This paper presents an investigation in the progressive failure mechanism of a large bedding slope with a strain-softening interface. For this purpose, the shear properties for the common types of weak interface are investigated through a series of repeated shear tests. After that, the user-defined Fish program embedded in the finite difference method FLAC is employed to develop a strain-softening constitutive model for the contact element based on the Mohr–Coulomb model. Then, a model for a large bedding slope with a strain-softening interface is established using the modified contact element in FLAC. It is noteworthy that the distribution of bedding planes and joint surfaces among the rock strata is also taken into consideration. Finally, the chain action law of strain softening is obtained through numerical analysis, based on which the progressive failure mechanism of a large bedding slope can be proposed. The feasibility of the strain-softening and the progressive failure mechanism of bedding slopes proposed in this paper are validated combining a typical case in Yiwan Railway Route.

## Laboratory investigation of the interface

The interfaces among the rock stratums are often filled with strain-softening geotechnical materials (Indraratna et al. 2014; Li et al. 2014; Sinha and Singh 2000). As one of the most common types of weak interfaces, the mudded weak interlayer is considered to be the most dangerous slip surface. To obtain the progressive failure mechanism of a large bedding slope with a strain-softening interface, it is essential to investigate the shear properties of the interfaces, i.e., the mudded weak interlayer.

### Specimen preparation

The shear behavior of the mudded weak interlayers can be studied through repeated direct shear tests (Bahaaddini et al. 2013). According to a large number of site investigations for bedding slopes in Southwest China, the rock stratum of theses slopes are mainly mudstone, carbonate

rock and charcoal shale with the approximate proportions of 61, 17 and 22%, respectively (Wang et al. 2013; Zheng 2012). In order to ensure the popularity and representation of the test data, the specimens tested in this paper are divided into three types accordingly.

For the mudded weak interlayer in the mudstone, the specimens were obtained from a bedding slope along the Cheng-Jian Express Way in Southwest China (N:30.497207°, E:104.336521°), where red mudstone is widely developed. As shown in Fig. 1a, b, the specimens were collected by cutting ring samples and labeled in line with the dislocation direction. Afterwards, all the specimens were sealed with wax (Fig. 1c) and kept in a water-retention box (Fig. 1d) to keep them undisturbed.

In the same way, the mudded weak interlayer specimens in rock stratum of carbonate and charcoal shale were collected from bedding slopes located at a highway slope in Jiangyou City, Sichuan Province (N:32.077264°, E:105.073267°) and the Yu Xiang Expressway, Southwest China (N:29.353115°, E:108.766790°), respectively. Figure 2 shows the general view of the sampling site slope and the development condition of mudded weak interlayer in rock stratum of carbonate and charcoal shale.

## Testing procedure

According to the related test specifications (XP 1997), a strain-controlled direct shear apparatus was used to perform repeated shear tests on the slip surfaces. The specimens were sheared under vertical stresses of 50, 100, 150 and 200 kPa at a shear rate of 0.02 mm/min. When the shear stress exceeded the peak, the shear displacement was recorded every 0.5 mm until the total displacement reached 5–8 mm. Upon finishing the first shear process, the upper shear box was pushed back in reverse at a rate of 0.6 mm/min. The process was repeated until the last two readings of the stress sensor were approximately equal. Figure 3 shows the brief shear process of the mudded weak interlayer specimens.

## Testing results and discussion

As a typical example, the shear stress–displacement curves of the repeated shear tests under a vertical stress of 50 kPa are shown in Fig. 4.

Neglecting the initial line elastic deformation segment, the other data plots are fitted using the least squares method. All the shear stress–displacement curves for the three kinds of weak interlayer under different vertical stresses are shown in Fig. 5, and the peak and residual shear stresses as functions of the vertical stresses are obtained.

It can be seen from Fig. 5 that all the specimens under different vertical stresses share the characteristic of strain softening. First, the shear stress increases linearly with the displacement before the peak. After that, the shear stress begins to decrease until a relatively stable state is reached, which is called the residual stage. In addition, both the peak and residual shear stresses have positive correlations with the vertical stresses.



**Fig. 1** Collection process of the mudded weak interlayer specimens

**Fig. 2** General view of the sampling site slope and the development condition of the mudded weak interlayer in rock stratum of carbonate (**a**) and charcoal shale (**b**)
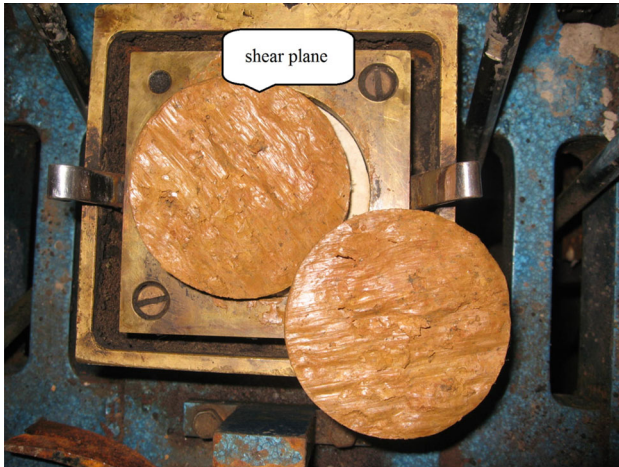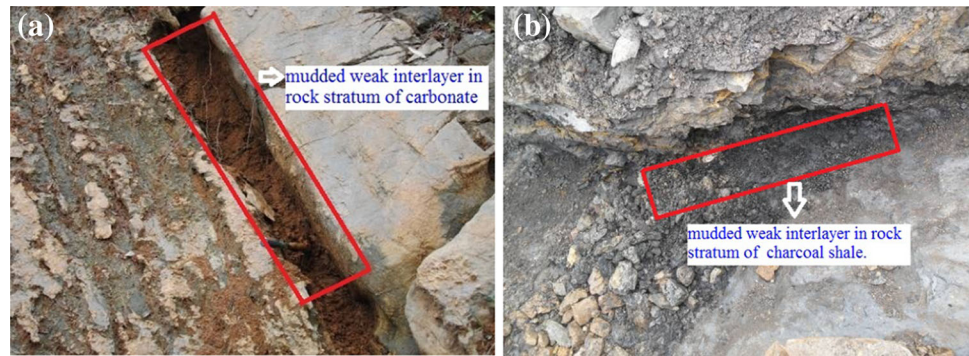


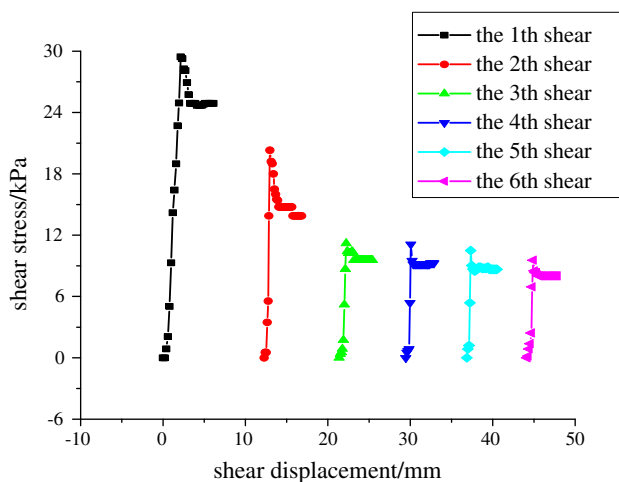**Fig. 3** Shear plane of the mudded weak interlayer specimen



**Fig. 4** Results of repeated shear tests under the vertical stress of 50 kPa

## Modeling the strain-softening interface

Laboratory test results suggest that the interlayers among the rock strata in bedding slopes share the characteristic of strain softening (Chai et al. 2007). To simulate an interface with this shear trait, the user-defined Fish program in FLAC can be employed to develop a constitutive model of the contact element based on the Mohr–Coulomb model (Wang et al. 2013; Zheng 2012). As a finite difference software, FLAC is widely used in geotechnical engineering (Wang et al. 2011; Xiumina et al. 2012; Xuegui et al. 2011). In this section, the method to simulate the strain-softening contact element is presented in detail as follows.

### Contact element with the strain-softening constitutive model

The contact constitutive model in the present study is based on the tri-linear strain-softening model (Toshikazu 1981). That is, only the elastic deformation occurs in the contact element when a small shear stress acts on it. In this stage, the strength parameters remain steady at their peak values ($\varphi_p$, $c_p$). The strain-softening stage would not appear until the shear stress exceeds the maximum value, as calculated through the Mohr–Coulomb criterion. During the softening stage, both the cohesion c and internal friction angle $\varphi$ decay with the increase of the plastic shear displacement. Figure 6 shows the common types of strain softening (a) and shear strength reduction (b). It is discovered from Fig. 6b that the strength parameters (c, $\varphi$) reduce to the residual shear strength ($c_r$, $\varphi_r$) when the plastic shear displacement reaches $L_p$.

Thus, the constitutive model of the contact element can be established through the following steps. First, in each time step of FLAC, imem ($i$) and fmem ($i + j$) in Fish program are called to extract the maximum shear stresses of all the contact elements and the relative shear strains of all the contact nodes, where $i$ is the address pointer and $j$ is the offset of the address pointer (Itasca 2005). Second, the extracted stresses and strains of each time step were used for comparison with the pre-defined strain-softening curve and strength reduction mode (as shown in Fig. 6). As a result, the corresponding strength parameters should be reduced if the contact point displacements of the element have entered into the plastic stage.
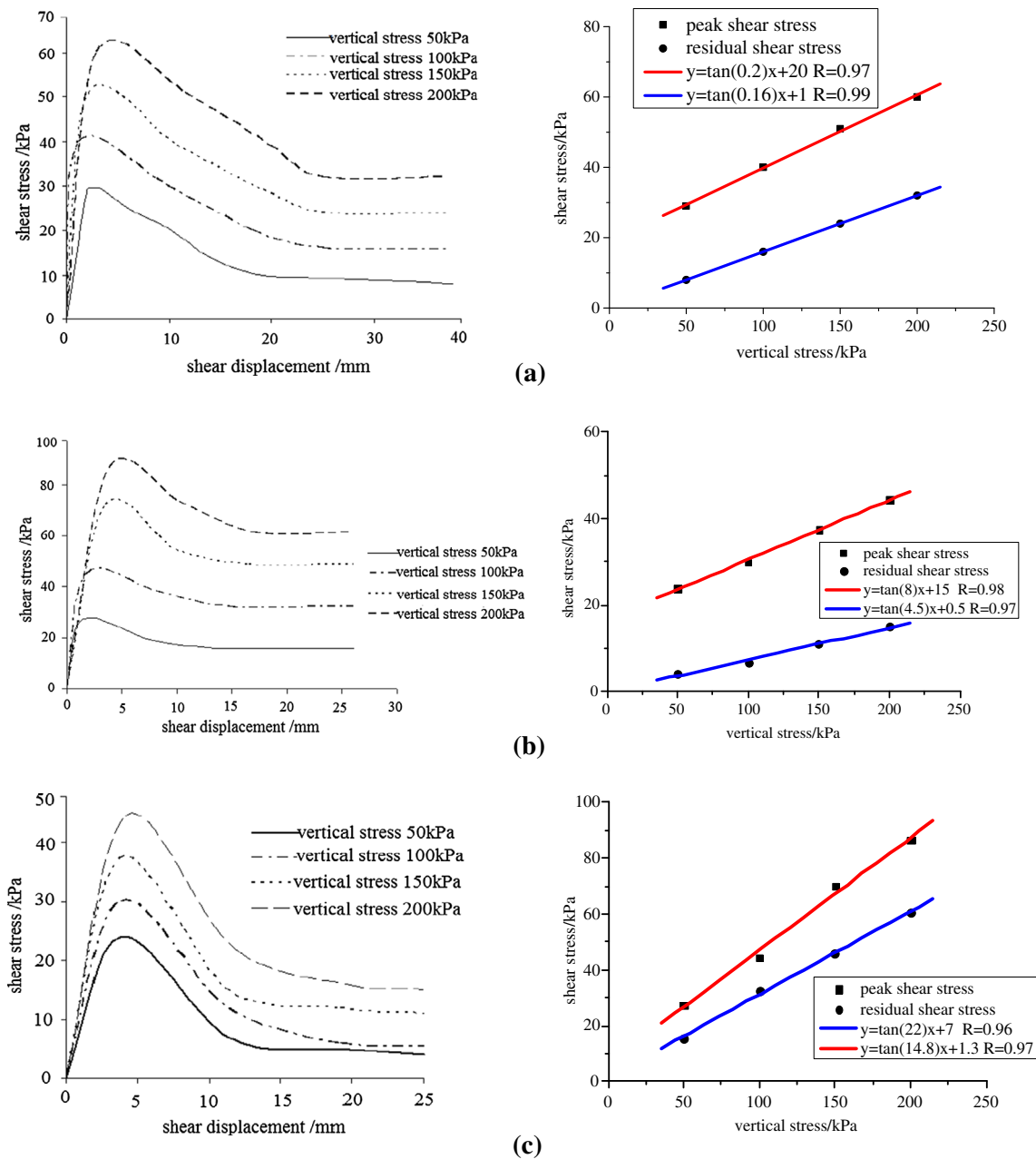
**Fig. 5** Shear stress–displacement curves under different vertical stresses and the peak and residual shear stresses as functions of the vertical stresses for the mudded weak interlayers in the stratum of mudstone (**a**), carbonate (**b**) and charcoal shale (**c**)

## Numerical verification

Laboratory experiments, especially direct shear tests, are common methods to obtain the strength parameters of the weak structural surface (Li et al. 2015). The existing research investigations indicate that the shear process of the interface is progressive because of its ubiquitous softening characteristics. To ensure the validity of the strain-softening contact element mentioned in "Contact element with the strain-softening constitutive model", the direct shear test simulated in FLAC with the user-defined

constitutive model is compared with the overall process of the laboratory test.

1. Numerical model set up

According to the actual dimensions of the laboratory direct shear test, the length of the model is 60 mm and the height is 20 mm. As shown in Fig. 7, the model is divided into two symmetrical parts by the interface. The simulation of the interface is accomplished by a total of 20 contact elements (no. 1–20), each of which has a length of 3 mm. On both sides of the interface, 200 solid elements are

**Fig. 6** Common types of strain softening (**a**) and shear strength reduction (**b**)
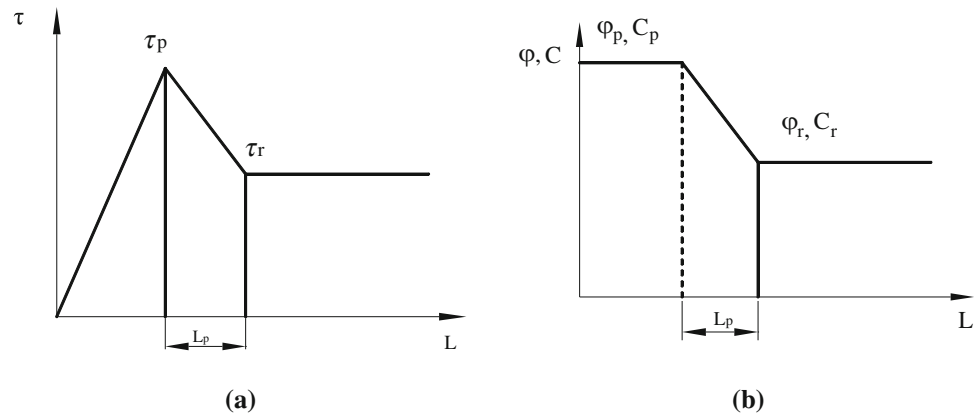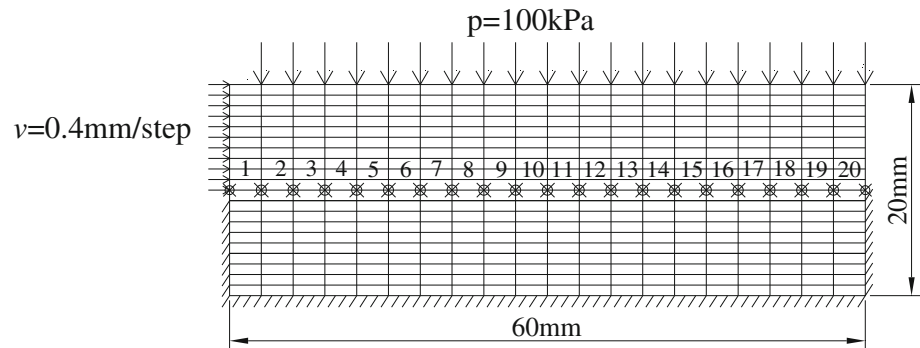


**(a)**

**(b)**

**Fig. 7** Numerical model of direct shear test



established. Following that, uniformly distributed loads of 100 kPa are applied to the top surface of the model. Displacement-controlled loading is adopted to apply the horizontal shear force, and the load velocity is set as 0.4 mm per time step.

The constitutive model for the solid element is set as the Mohr–Coulomb model, and the material parameters are shown in Table 1. Specifically, for the interface element, four common types of constitutive model are taken into consideration, including the non-softening model (that is, the Mohr–Coulomb model), the friction angle softening model, the cohesion softening model and the general softening model. It is noteworthy that the non-softening model is divided into three types according to the different strength parameters, i.e., the non-softening model 1 (only the cohesion is considered), the non-softening model 2 (only the friction angle is considered) and the non-softening model 3 (both the cohesion and friction angle are

**Table 1** Model parameters of the solid elements in the direct shear test simulation

| Unit weight $\gamma$ (kN/m$^3$) | $K$ (Pa) | $G$ (Pa) | Internal friction angle (°) | Cohesion (kPa) |
|---|---|---|---|---|
| 26 | 2e7 | 1e7 | 50 | 100 |

considered). The general softening model mentioned above takes both the friction angle and cohesion into account.

In this section, some essential parameters of the contact elements are needed to perform the numerical shear tests, such as the contact stiffness and strength parameters, aiming at the validation of the user-defined constitutive model of the contact element. During direct shear test simulation, the realization of strain-softening characteristics at the interface is given the most concern. The peak and residual strength parameters (i.e., the cohesion c and internal friction angle $\varphi$) for the four types of softening models are different while the shear stiffness ks and normal stiffness kn of the contact element is constant. Goodman et al. (1968) introduced the terms "normal stiffness" ($k_n$) and "shear stiffness" ($k_s$) to describe the changing rates of stresses (normal stress and shear stress) with respect to displacements (normal displacements and shear displacements). Accordingly, the shear stiffness $k_s$ and normal stiffness $k_n$ can be determined through the direct shear tests and uni-axial compression tests, respectively.

Figure 8a, b show the test results of the direct shear and uni-axial compression on the mudded weak interlayer specimens, respectively. The $k_n$ and $k_s$ of each specimen can be determined by the ratio of stress before the peak (normal stress and shear stress) and corresponding displacement (normal displacements and shear displacements). In order to
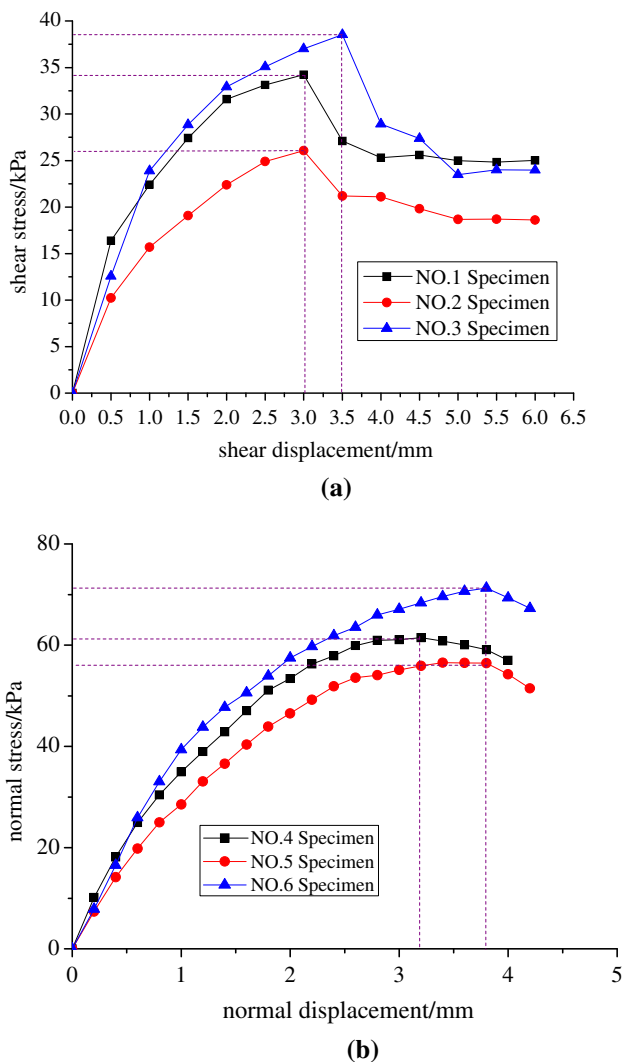
Fig. 8 The test results of the direct shear (a) and uni-axial compression (b) on the mudded weak interlayer specimens

**Table 2** The direct shear test results of the shear stiffness $k_s$

| Sample ID | No. 1 | No. 2 | No. 3 |
|---|---|---|---|
| Shear stress (kPa) | 34.00 | 26.20 | 38.60 |
| Shear displacement (mm) | 3.00 | 3.00 | 3.50 |
| Shear stiffness $k_s$ (Pa/m) | 1.33e7 | 0.87e7 | 1.10e7 |
| Average value of the $k_s$ (Pa/m) | 1.10e7 | | |

**Table 3** The uni-axial compression test results of the normal stiffness $k_n$

| Sample ID | No. 4 | No. 5 | No. 6 |
|---|---|---|---|
| Normal stress (kPa) | 61.50 | 57.00 | 71.50 |
| Normal displacement (mm) | 3.20 | 3.20 | 3.80 |
| Estimation of the $k_n$ (Pa/m) | 1.92e7 | 1.78e7 | 1.88e7 |
| Average value of the $k_n$ (Pa/m) | 1.86e7 | | |

get a more reasonable estimation of the shear stiffness, the final $k_s$ and $k_n$ are determined through the arithmetic mean value of the three parallel specimens, as shown in Tables 2 and 3, respectively.

It can be known from Tables 2 and 3 that the estimating values of the shear stiffness and normal stiffness are 1.10e7 and 1.86e7 Pa/m, respectively. However, they may not be eventual stiffness values of the interface. Instead, the appropriate $k_s$ and $k_n$ are finally adjusted by numerical trial tests in FLAC. The numerical simulation results can be in good agreement with the laboratory test results when $k_s = 1e7$ and $k_n = 2e7$ Pa/m. The parameters of the four different constitutive models are listed in Table 4.

(2) Results and discussion

Figure 9 shows the simulation results of the different constitutive models listed in Table 4. It is discovered from

the shear stress–displacement curve in Fig. 9a that the shear stresses of the non-softening model hold steady after the peak. On the other hand, when the softening model is defined, the shear stresses experience a reduction after the peak, as shown in Fig. 9b. For different strain-softening parameters, the attenuation slopes and residual values differ from each other. In general, the simulation results for different types of constitutive models are in good accordance with the data in Table 4, which means that the method to simulate the strain-softening interface with the contact elements mentioned above is feasible.

(3) The progressive failure process of the interface

To obtain the transfer rule of internal stress at the interface, the stresses of the contact elements numbered from 1 to 20 of both the non-softening model and softening model are monitored in FLAC. The shear and normal stresses of the non-softening model and softening model as functions of the time steps are shown in Figs. 10 and 11, respectively.

It can be learned from Figs. 10a and 11a that the distributions of the normal stresses for both models are non-uniform. To begin with, the normal stress of the contact element next to the horizontal loading surface increases rapidly when the shearing begins. During the process of shearing, the maximum normal stress point moves from the loading side towards the other side, leading to a smaller front and greater posterior. It is notable that the normal stress of the non-softening model ultimately reaches a relatively steady state, while that of the softening model gradually regresses with the increase in the number of time steps.

As shown in Figs. 10b and 11b, the evolution law of the shear stress can be summarized. At the beginning, the shear

**Table 4** Model parameters of the contact elements in the direct shear test simulation

| Type of contact element | $k_n$ (Pa/m) | $k_s$ (Pa/m) | $c_p$ (kPa) | $c_r$ (kPa) | $\phi_p$ (°) | $\phi_r$ (°) | $L_{pc}$ (cm) | $L_{p\phi}$ (cm) |
|---|---|---|---|---|---|---|---|---|
| Non-softening model 1 | 2e7 | 1e7 | 40 | 40 | 0 | 0 | – | – |
| Non-softening model 2 | 2e7 | 1e7 | 0 | 0 | 30 | 30 | – | – |
| Non-softening model 3 | 2e7 | 1e7 | 40 | 40 | 30 | 30 | – | – |
| Friction angle softening model | 2e7 | 1e7 | 0 | 0 | 30 | 10 | – | 1 |
| Cohesion softening model | 2e7 | 1e7 | 40 | 5 | 0 | 0 | 1 | – |
| General softening model | 2e7 | 1e7 | 40 | 5 | 30 | 10 | 1 | 1 |
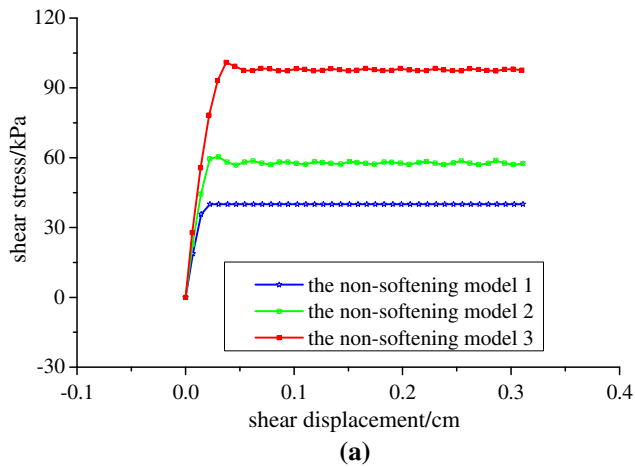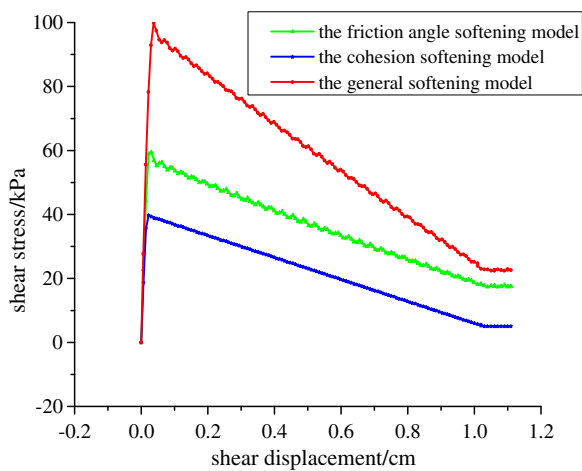


**Fig. 9** Shear stress–displacement curves for the non-softening model (**a**) and strain-softening model (**b**)



**Fig. 10** Normal stress (**a**) and shear stress (**b**) of the contact elements from no. 1 to no. 20 as functions of the time steps in the non-softening model

stress increases linearly until reaching its peak, and the growing rate is dependent on the shear stiffness. The stress concentration first occurs at a position near the loading surface. Subsequently, it gradually transfers from the front to the middle and posterior of the model, which leads to the formation of a maximum shear stress region at the posterior of the model. For different interface models, the evolution

law of shear stress shows distinguishing characteristics. When the interface model is set as the non-softening model, similar to the normal stress, the shear stress reaches a certain value. Instead, if the strain-softening contact element is selected, the strength reduction caused by the shear dislocation should be taken into consideration. According to the numerical computation of the general softening model described in Table 4, the tendency of the
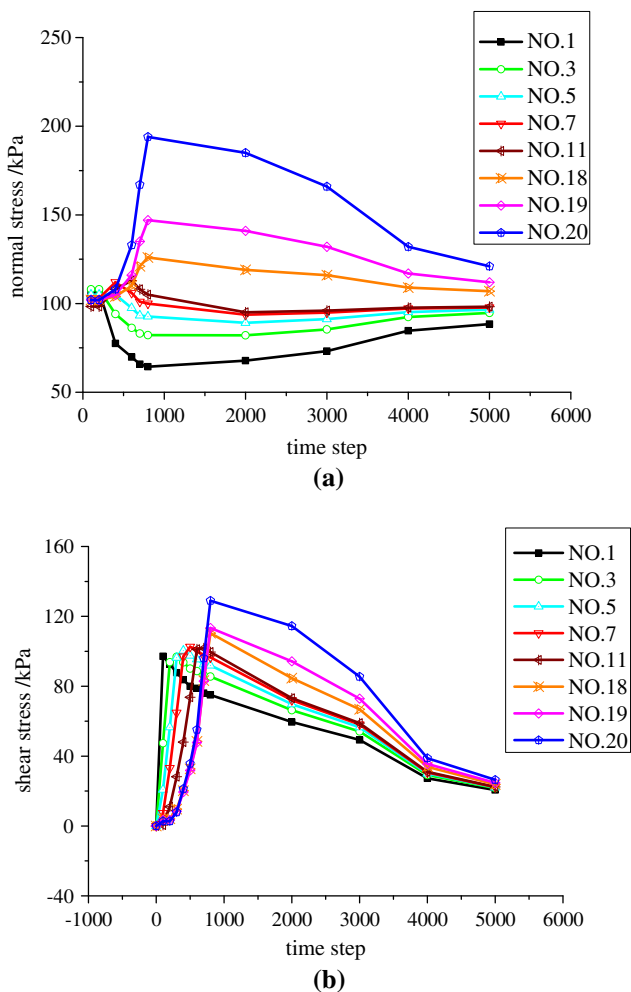
Fig. 11 Normal stress (a) and shear stress (b) of the contact elements from no. 1 to no. 20 as functions of the time steps in the softening model

shear strength reduction with the time step increasing can be seen in Fig. 12.

## Progressive failure mechanism of a large bedding slope

### Models of the bedding slope

A large bedding slope with complex bedding planes and vertical joints is considered in this study. To simulate the strain-softening effect of the bedding planes among the rock stratums, the contact element mentioned in "Modeling of Strain-Softening Interface" is applied to the following model in FLAC.

To simplify the computation, a compound slope model with a single bedding plane and several vertical joints is established based on site experience. As shown in Fig. 13,
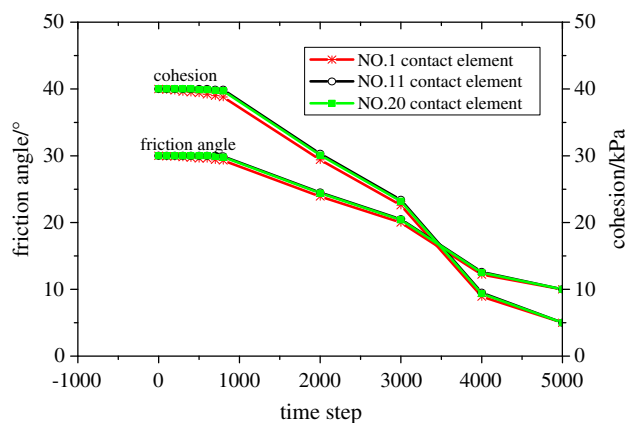


Fig. 12 Typical reduction model for the friction angle (a) and cohesion (b) reduction with the time step increasing

the thickness of the upper rock strata is set as 6 m, and the horizontal projection of the slope length is set as 300 m. The spacing between adjacent joint surfaces is 4 m. Taking full consideration of size effect in the numerical simulation, both sides of the slope model are extended with a length of 300 m. Specifically, it is known that the inclination angle plays an important role in the slope stability, and the present study is mainly concerned with low inclination angle slopes. Therefore, the inclination angle of the rock strata is set as 25°. Additionally, there are 12,496 elements of rock mass and 540 contact elements created in this numerical model.

As shown in Fig. 14, the bedding planes and vertical joint surfaces are represented by contact elements. It must be mentioned that the contact constitutive models of the vertical joint surfaces are set as per Mohr–Coulomb, while the bedding planes are set based on the strain-softening contact models, as mentioned above. The constitutive model of the rock mass is the Mohr–Coulomb model, and the material parameters of the rock mass and contact elements are listed in Table 5. According to the testing results in "Laboratory Investigation of the Interface", the characteristic parameters of strain softening for the bedding planes can be seen in Table 6.

### Response of the contact elements to interlaminar stresses

To investigate the effect of the strain-softening contact element on the interlaminar stress, the initial stress characteristics of the bedding plane should be calculated. In this stage, the strength parameters of the contact element stay at the peak ($\varphi_p = 20°$, $c_p = 15$ kPa) because the strain softening does not occur. Figure 15 shows the curves of the shear and normal stresses as functions of the slope length before the strain-softening effect.

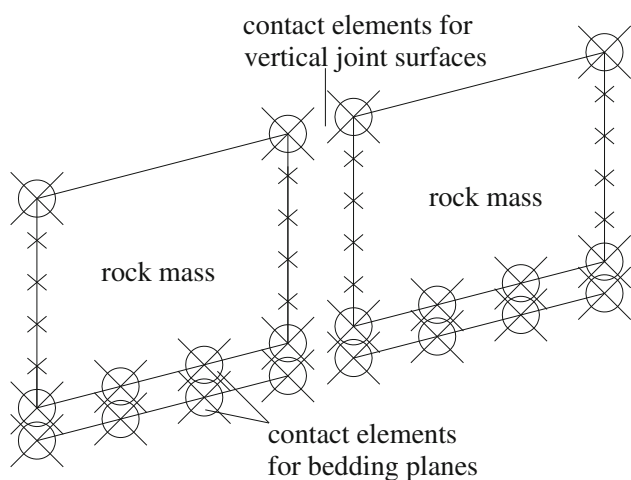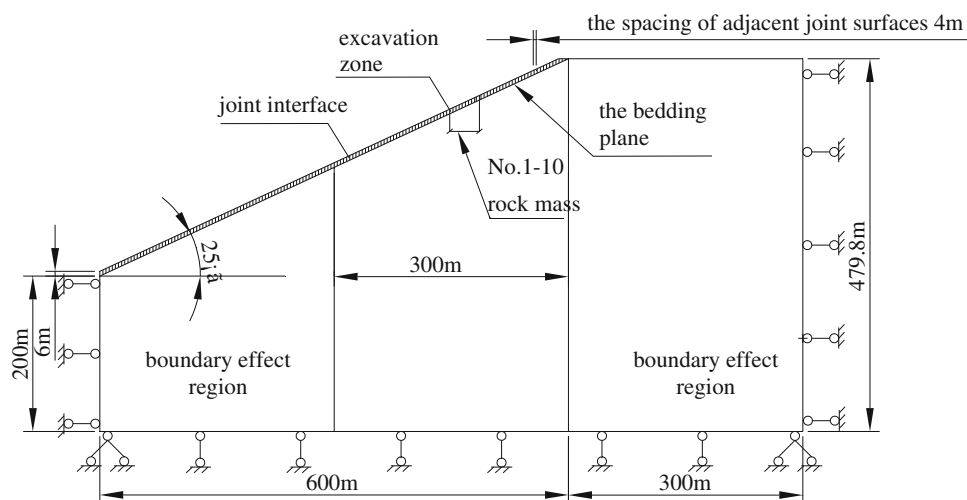Fig. 13 Geometric model of the large consequent slope



Fig. 14 Setting of contact elements in the model



**Table 5** Material parameters of the rock mass and contact elements in the direct shear test simulation

| Element types | Unit weight (kg/m$^3$) | Deformation parameter | | Strength parameter | |
|---|---|---|---|---|---|
| | | $G$ (GPa) | $K$ (GPa) | $\varphi$ (°) | $C$ (kPa) |
| Rock mass | 26 | 1 | 2 | 60 | 1000 |
| Contact element of bedding plane | – | 0.01 | 0.02 | 20 | 15 |
| Contact element of vertical joint surface | – | 0.1 | 0.1 | 25 | 0 |

**Table 6** Characteristic parameters of strain softening for the bedding planes

| Element parameters | $\varphi_p$ (°) | $\varphi_r$ (°) | $C_p$ (kPa) | $C_r$ (kPa) | Plastic shear displacement $L_m$ (mm) |
|---|---|---|---|---|---|
| Contact element | 20 | 16 | 15 | 2 | 3 |

the interlaminar stress, a distinct shear stress concentration occurs at the toe of the slope, while the normal stress hovers relatively steady at 120 kPa.

Because of the different shear stress characteristics mentioned above, the contact elements are in different stages of strain softening. When the shear stress is small, only elastic deformation occurs in the contact elements, and the strength parameters keep steady at the peak ($\varphi_p = 20°$, $c_p = 15$ kPa). However, the shear stress of some contact elements may reach the maximum and can be described as

$$\tau_p = c_p \cdot l + \sigma_n \cdot \tan\varphi_p, \tag{1}$$

where $c_p$ and $\varphi_p$ are the peak cohesion and friction angle of the contact element, respectively. $l$ denotes the length of a contact element, and $\sigma_n$ denotes the normal stress. As the computing time increases, the strength parameters ($c$, $\varphi$) begin to reduce once the shear stress of the contact element has exceeded its maximum stress $\tau_p$. After the plastic shear displacement has reached 3 mm, the shear stress decreases from the peak to the minimum stress $\tau_r$. The strength parameters also reduce to the residual value ($\varphi_r = 16°$, $c_r = 2$ kPa).

After the strain softening stage occurs in the stress concentration area, the strength parameters along the bedding plane are no longer uniformly distributed. Figure 16 shows the new characteristics of the distributions of the

It may be observed in Fig. 15 that neither the shear nor the normal stresses are uniformly distributed below the single rock mass. Stress concentrations appear at the cuspidal points of all the rock masses and decrease gradually towards the posterior. According to the macro-analysis of
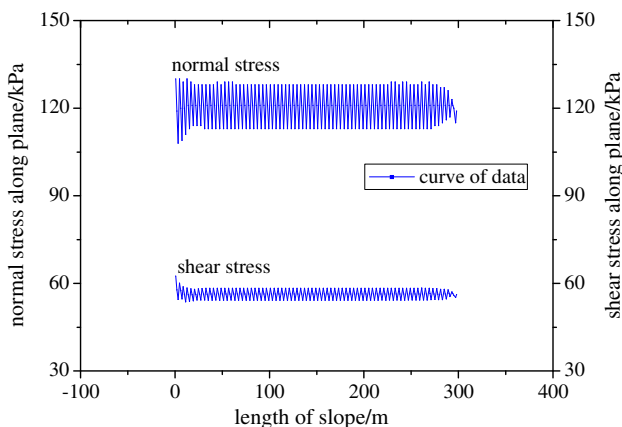
Fig. 15 Curves of the shear stress and normal stress as functions of the slope length before the strain-softening effect
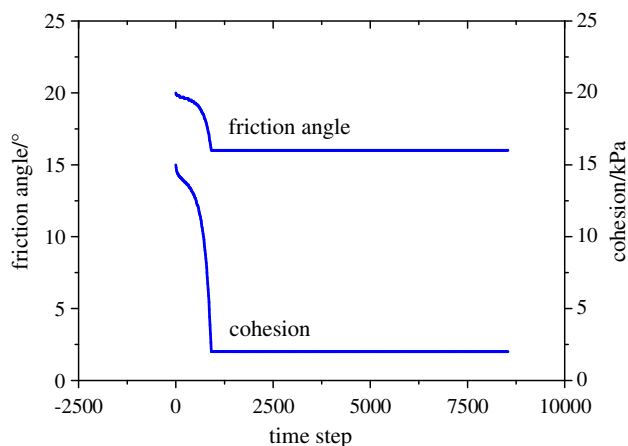


Fig. 17 Friction angle and cohesion of the contact element as functions of the time step
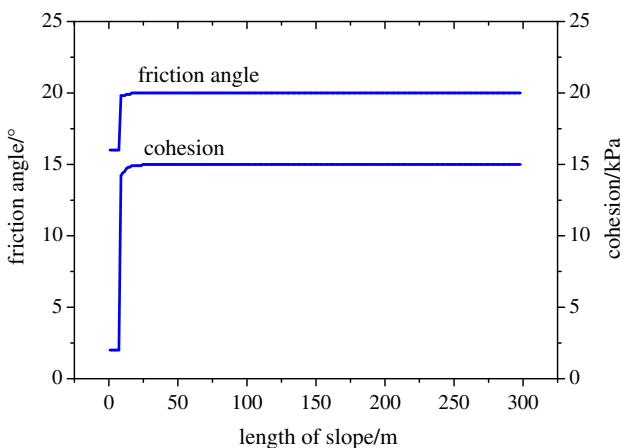


Fig. 16 Distribution of the friction angle and cohesion along the bedding plane
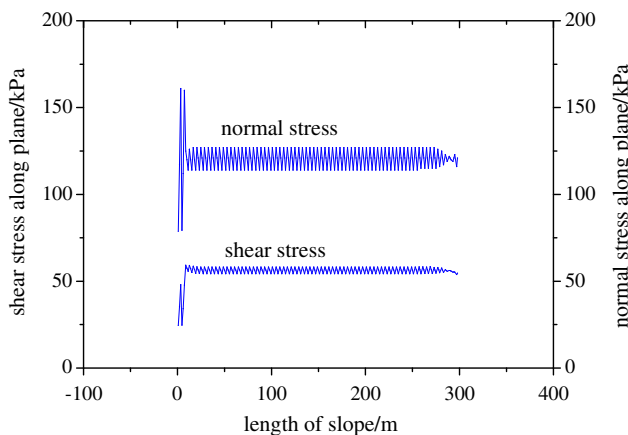


Fig. 18 Shear stress and the normal stress along the bedding plane after the strain-softening effect

cohesion and friction angle. The shear strength of the contact element below the first rock mass near the slope toe is monitored during the entire process, and the results are shown in Fig. 17.

It can be observed in Fig. 16 that the strength reduction induced by strain softening starts at the contact element of the first rock mass. To be specific, the friction angle reduces to 16° from 20°, while the cohesion reduces to 2 from 15 kPa, as shown in Fig. 17. Both the friction angle and cohesion decrease to their minima at the time step of 1000.

Compared to the initial stress condition described in Fig. 15, the stresses along the bedding plane have undergone great changes. As shown in Fig. 18, the shear stress of the contact element below the first rock mass also decreases to approximately 30 kPa due to the strain softening, and the normal stress exhibits a very large fluctuation. In particular, the area of stress concentration gradually transfers to the next rock mass.

## Progressive failure mode

The response of the contact elements to the interlaminar stresses will extend to the entire bedding plane in the form of a chain reaction, which plays an important role in the failure mode of the large bedding slope.

To obtain the failure characteristics of the large bedding slope from the effect of strain softening, the displacement of the slope is investigated in detail. According to the simulation results, the failure process can be divided into two main stages, which are shown in Figs. 19 and 20.

In the first stage, as shown in Fig. 19, the progressive loosening of the rock mass first occurs near the free surface and gradually extends to the next one in the first stage. According to the numerical results, the maximum loosened region at the time step of 2000 has a length of 16 m, and the corresponding horizontal displacement is 0.175 m. At time step 6000, the length of the maximum loosened region increases to 28 m, and the maximum horizontal
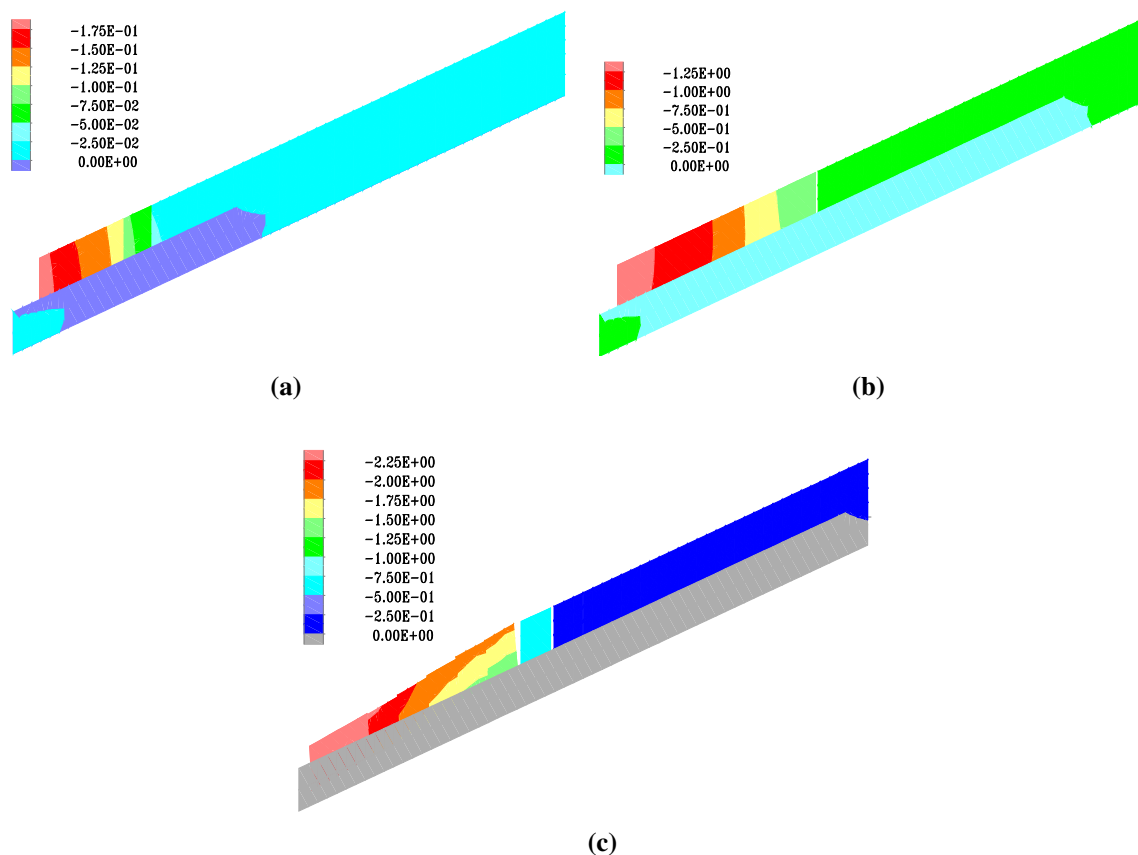
**Fig. 19** Evolution law of the horizontal displacement in the first stage at the time steps of 2000 (**a**), 6000 (**b**) and 10,000 (**c**)

displacement is 1.25 m. The maximum loosened region of the slope no longer broadens for the moment; instead, it experiences internal sliding-tensile fracturing. With the further increase in the time steps, the sliding-tensile deformation intensifies sharply until it exceeds the limitation of the contact elements. To ensure the validity of the subsequent simulation, the part of the model that exceeds the maximum deformation limitation must be deleted automatically. Finally, this stage ends with the integral slippage of the region that consists of several rock masses.

In the second stage, the single rock mass is progressively destabilized in a loop. It can be concluded from Fig. 20 that none of the destabilizations appear in the form of the overall structural failure of several rock masses. Instead, the failure continues primarily with a single rock mass, and the failure process is cyclic without any change in stress. The cyclic process before the final failure often lasts a long time. Figure 21 shows the final state of the large bedding slope.

**Stress field features along the bedding plane**

To further investigate the progressive failure mechanism, the shear and normal stresses of the contact elements along the bedding plane are monitored during the whole process. Figure 22a shows the monitoring results of the shear stresses below nos. 1–10 rock mass, and Fig. 22b plots the maximum shear stresses as functions of the horizontal position. It may be observed that the distribution of the stresses along the bedding plane exhibits two stages. In the first stage, the rock masses from no. 1 to no. 7 share a similar shear stress evolution law, where the shear stress first increases linearly and then quickly attenuates until it fluctuates around a constant value. However, in the other region (beyond 28 m), there is no significant increase in the shear stress, but instead it rapidly decreases to a relatively stable value.

**Failure mechanism**

Through the numerical simulation results, the failure mechanism of a large bedding slope with a strain-softening interface can be concluded to be as follows:

To begin with, the shear stresses concentrate at a point near the free surface. Controlled by the strain-softening characteristics of the bedding plane (interface), strength reduction occurs in the stress concentration region. Thus, the weakening of the region caused by
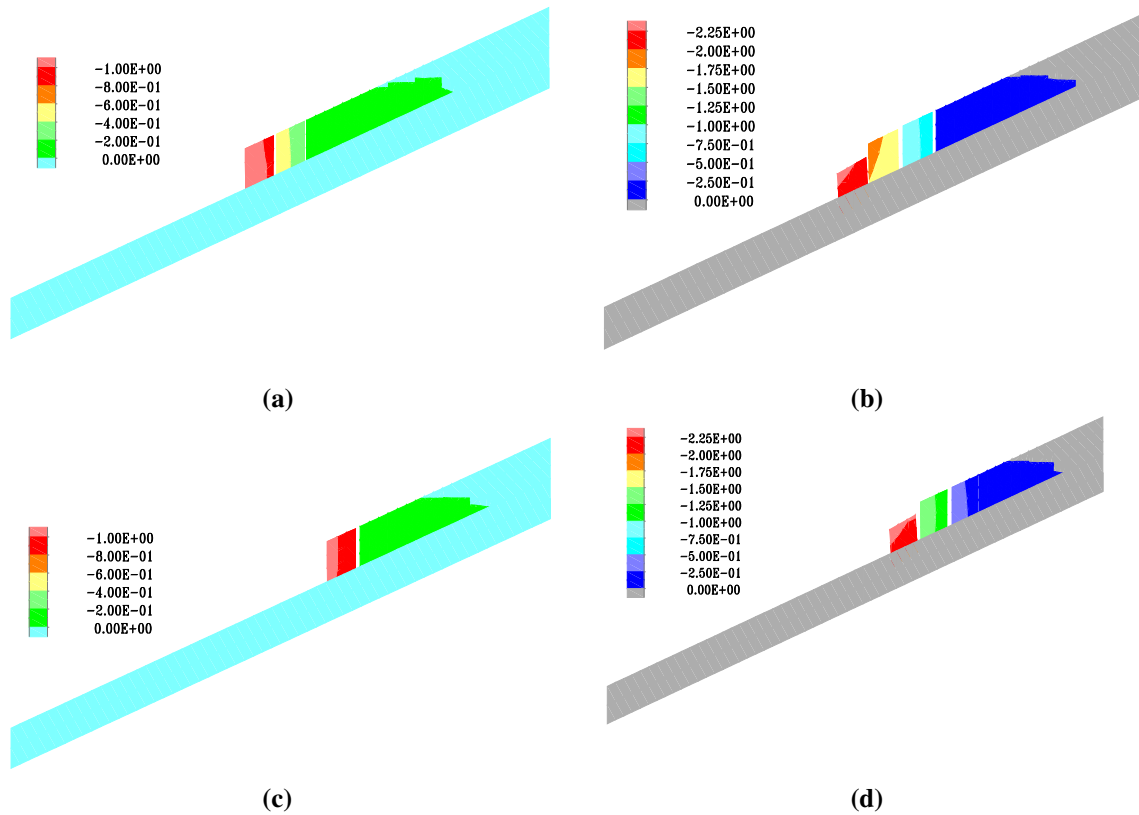
**Fig. 20** Evolution law of the horizontal displacement in the second stage at the time steps of 12,000 (**a**), 16,000 (**b**), 20,000 (**c**) and 24,000 (**d**)
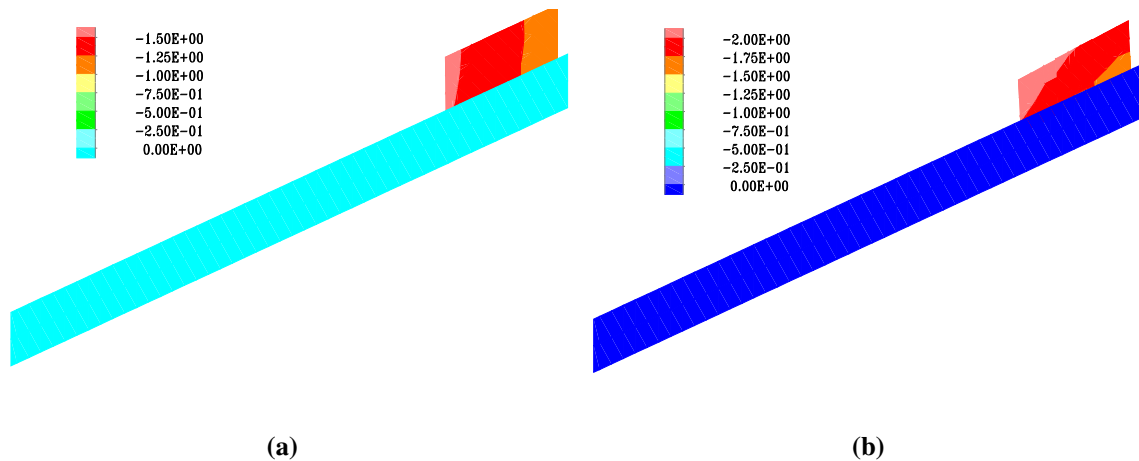


**Fig. 21** Final state of the large consequent slope model when the time step is 342,000 (**a**) and 344,000 (**b**)

strain softening finally results in the local failure of the toe segment.

After the local failure, the stress concentration of the subsequent bedding plane is not that distinct. Hence, the situation in which several rock masses are softened and destabilized all at once no longer happens. Instead, the failure is mainly converted to the destabilization of a single rock mass. Like the weathering of rock, the failure of the large bedding slope is a drawn-out and progressive process.

## Case study: a bedding slope locating at the Badong Railway Station, Yiwan Railway Route

In this section, a typical engineering case is investigated to validate the feasibility of the strain-softening contact element and the progressive failure mechanism of bedding slopes. Both the strain-softening and traditional Mohr–Coulomb contact elements are employed to simulate the bedding plane, respectively. Additionally, the simulation
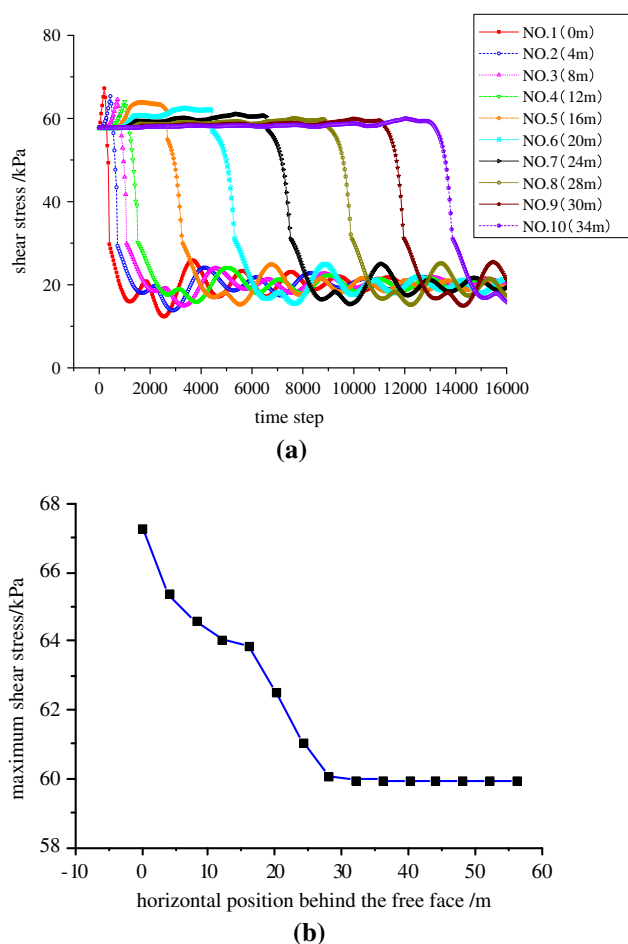
**Fig. 22** Monitoring results of shear stresses below the nos. 1–10 rock mass (**a**) and the maximum shear stresses as functions of the horizontal position (**b**)

results are compared with the field monitoring data to determine the optimal constitutive model of the contact element. It is important to note that it is dangerous, costly and impracticable to reproduce the failure process of large bedding slopes onsite. This slope along the Yiwan Railway Road has been reinforced by anti-slide piles, which means the failure process may not be observed directly. Instead, we can conclude the deformation law of the slope body after the slope excavation, which is helpful to analyze the possible failure mechanism.

### Site description and numerical model set up

This large bedding slope is located in Yeshanguan Town, Badong County in Hubei Province (N:30.661694°, E:110.354317°). According to the geological survey, the main rock of this bedding slope is charcoal shale, with the dip angle of 17°. The slope is excavated at the middle of the mountain. Meanwhile, the slope is inter-bedded with mudded weak interlayers, which possess the characteristic

of strain softening. A typical section of this slope is selected where the general dimension of the bedding slope can be seen in Fig. 23. Actually, the model can be divided into four major components, that is, the upper and lower rock mass (homogeneous charcoal shale), the mudded weak interlayer (strain-softening interface), vertical joint surface in the upper rock mass (with the spacing of 10 m) and the anti-slide pile. The upper and lower rock mass are simulated with the Mohr–Coulomb constitutive model. The joint surfaces in the upper rock mass are simulated with the Mohr–coulomb contact elements. Pile elements inside the FLAC are employed to simulate the anti-slide pile. For the interface between the upper and lower rock mass, both the Mohr–Coulomb and strain-softening contact element are used to perform the contrastive research. The specific parameters for the geo-materials and the anti-slide pile in this model are listed in Tables 7 and 8, among which the geo-material parameters are mainly obtained by in situ direct shear tests and laboratory shear tests. For the parameters of piles, they are quoted from the research results of Wang et al. (2013) and Zheng (2012).

### Simulation results under different conditions of the interface

When the Mohr–Coulomb contact element is defined, it means that only the peak strength is taken into consideration ($\varphi_p = 21°$). In this case, the deformation of the anti-slide pile and slope surface can be seen in Fig. 24. It can be learned from Fig. 24 that the maximum displacement of the pile is 2.513 mm, which is equal to the maximum deformation of the slope surface.

While the strain-softening contact element is applied to the bedding interface, the shear strength of the interface experiences a reduction from 21° to 13°, as shown in Table 7. Through the in situ direct shear tests and laboratory repeated shear tests, the plastic shear displacement of the mudded weak interlayer is determined as $L_p = 17.5$ mm. Figure 25 shows the deformation characteristics of the pile body and slope surface when the strain-softening contact element is employed. As a result, the maximum deformation occurs at the top of the free surface, with the value of 7.888 mm. The horizontal displacement of the anti-slide pile decreases linearly from the top to the anchor terminal.

### Validation of the strain-softening interface and progressive failure mechanism

The field monitoring results of horizontal displacement of the slope are compared with the numerical results, which can be seen in Fig. 26. It can be learned from Fig. 26 that

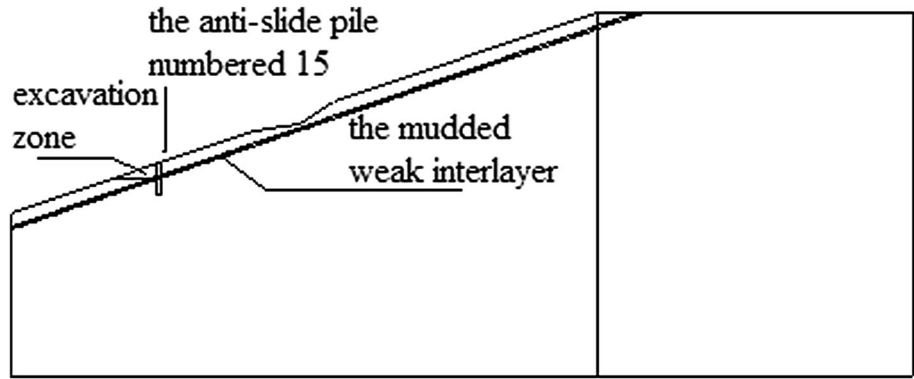Fig. 23 General view of the bedding slope in Badong Railway Station, Yiwan Railway Road

Table 7 The material parameters of the rock mass and contact elements in the numerical simulation

| Element types | Unit weight (kg/m³) | Deformation parameter | | Strength parameter | | | | |
|---|---|---|---|---|---|---|---|---|
| | | $E$ (GPa) | $\upsilon$ | $\Phi_p$ (°) | $C_p$ (kPa) | $\Phi_r$ (°) | $C_r$ (kPa) | $L_p$ (mm) |
| Rock mass | 22 | 6.7 | 0.25 | 42 | 700 | – | – | – |
| Contact element of bedding plane | – | 3 | 0.3 | 21 | 0 | 13 | 0 | 17.5 |
| Contact element of vertical joint surface | – | 0.1 | 0.1 | 25 | 0 | 25 | 0 | – |

Table 8 The parameters of the anti-slide pile

| Parameters | Value | Parameters | Value |
|---|---|---|---|
| Elasticity modulus (pa) | 2.54E+10 | Normal coupling stiffness (N/m/m) | 1.0E+09 |
| Pile length (m) | 20 | Normal coupling cohesion strength (N/m) | 1.0E+08 |
| Pile width (m) | 2.25 | Normal coupling friction angle (°) | 0 |
| Tangential coupling stiffness (N/m/m) | 1.3E+12 | Normal coupling tensile strength (N/m) | 0 |
| Tangential coupling cohesion strength (N/m) | 1.3E+08 | Perimeter of pile and soil (m) | 24.5 |
| Tangential coupling friction angle (°) | 30 | Pormal clearance of pile and soil (m) | 0 |
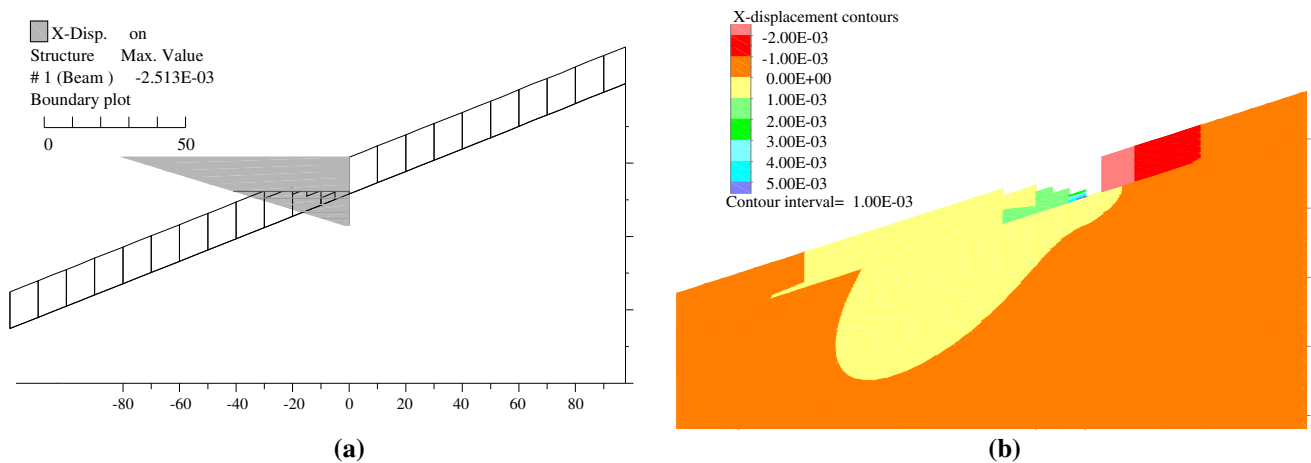


Fig. 24 Deformation of the anti-slide pile (a) and slope surface (b) when the Mohr–Coulomb contact element is set
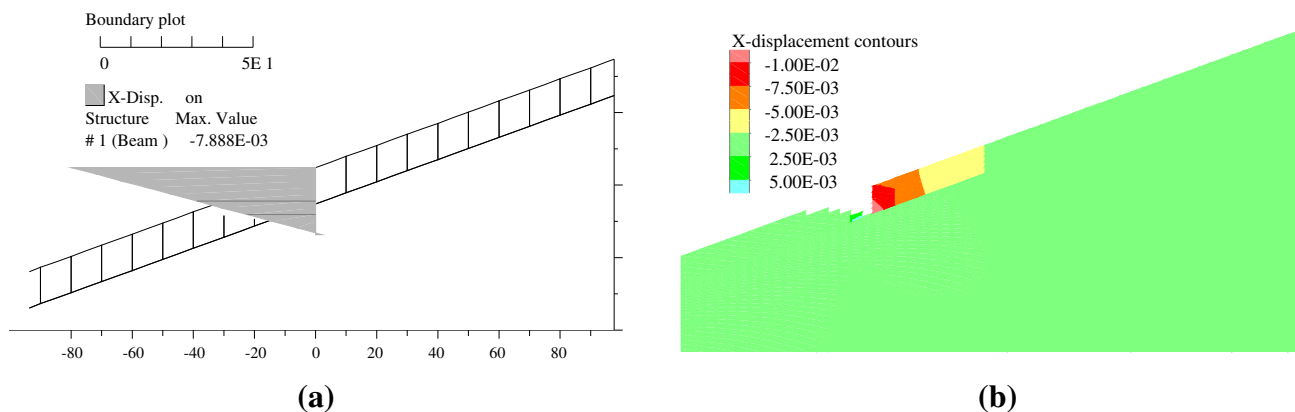
**(a)**                                                                              **(b)**

**Fig. 25** Deformation of the anti-slide pile (**a**) and slope surface (**b**) when the strain-softening contact element is set
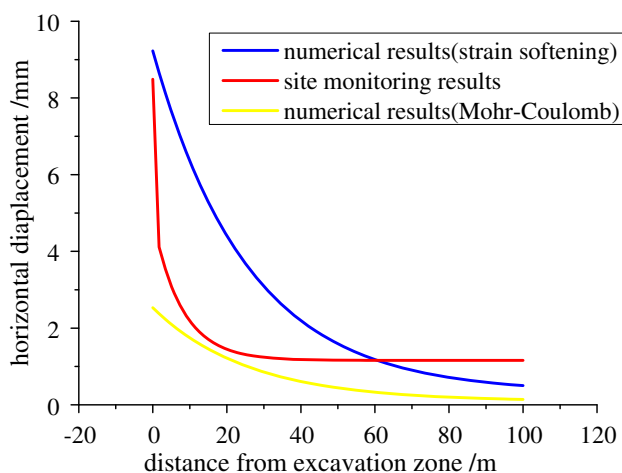


**Fig. 26** Comparison between the site monitoring results and the numerical results

the monitored deformation of the slope surface coincides better with the numerical results when the strain-softening contact element is applied. Thus, the strain-softening contact element is proved to be more feasible to simulate the bedding plane (with the mudded weak interlayer). Simultaneously, the major deformation concentrates at the section which is within 40 m from the free surface, which possibly illustrates that the failure process is progressive. Specifically, the slope may results in local failure of the toe segment firstly near the free surface and then the unstable segment will transfer to the rear end gradually.

## Conclusions

The mechanical behavior of a slope is strongly influenced by the strain-softening characteristics of the bedding plane. In this study, numerical tests have been conducted to study the progressive failure mechanism of a large bedding slope with a strain-softening interface.

To begin with, a contact element with the strain-softening constitutive model is developed in the finite difference method software FLAC to simulate the interface. Based on repeated laboratory shear tests, the validity of the contact element is verified. Afterwards, the contact element is applied to the numerical simulation of a large bedding slope with complex bedding planes and vertical joints. By investigating the response of the contact element to the bedding plane stress, the chained transfer rule of the strain softening is obtained. Finally, the failure characteristics of a large bedding slope with a strain-softening interface are concluded in combination with the numerical results. To be specific, the progressive failure process can be divided into two main stages, which include the local failure of the toe segment and the destabilization of the single rock mass. Through the case study of the large bedding slope located at Badong Station along the Yiwan Railway Route, both the user-defined contact element and the progressive failure mechanism of bedding slopes are verified.

## References

Bahaaddini M, Sharrock G, Hebblewhite BK (2013) Numerical direct shear tests to model the shear behaviour of rock joints. Comput Geotech 51:101–115

Białas M, Mróz Z (2005) Modelling of progressive interface failure under combined normal compression and shear stress. Int J Solids Struct 42(15):4436–4467

Chai JC, Carter JP (2009) Simulation of the progressive failure of an embankment on soft soil. Comput Geotech 36(6):1024–1038

Chai JC, Carter JP, Hayashi S (2007) Modelling strain-softening behaviour of clayey soils. Lowl Technol Int 9(2):29–37

Conte E, Silvestri F, Troncone A (2010) Stability analysis of slopes in soils with strain-softening behaviour. Comput Geotech 37(5):710–722

Eberhardt E, Stead D, Coggan JS (2004) Numerical analysis of initiation and progressive failure in natural rock slopes—the 1991 Randa rockslide. Int J Rock Mech Min Sci 41(1):69–87

Goodman RE, Taylor RL, Brekke TL (1968) A model for the mechanics of jointed rocks. J Soil Mech Found Div 94:637–659

Guo SF, Qi SW (2015) Numerical study on progressive failure of hard rock samples with an unfilled undulate joint. Eng Geol 193:173–182

Indraratna B, Premadasa W, Brown ET, Gens A, Heitor A (2014) Shear strength of rock joints influenced by compacted infill. Int J Rock Mech Min Sci 70:296–307

Itasca FLAC (2005) Fast Lagrangian analysis of continua v. 5.0. User's manual, Itasca Consulting Group, Minneapolis

Khan YA, Jiang JC, Yamagami T (2002) Progressive failure analysis of slopes using non-vertical slices. Landslide 39(2):203–211

Lee DH, Yang YE, Lin HM (2007) Assessing slope protection methods for weak rock slopes in Southwestern Taiwan. Eng Geol 91(2):100–116

Li YP, Liu W, Yang CH, Daemen JJK (2014) Experimental investigation of mechanical behavior of bedded rock salt containing inclined interlayer. Int J Rock Mech Min Sci 69:39–49

Li WF, Bai JB, Cheng JY, Peng SYD, Liu HL (2015) Determination of coal–rock interface strength by laboratory direct shear tests under constant normal load. Int J Rock Mech Min Sci 77:60–67

Mohammadi S, Taiebat HA (2013) A large deformation analysis for the assessment of failure induced deformations of slopes in strain softening materials. Comput Geotech 49:279–288

Roy S, Mandal N (2009) Modes of hill-slope failure under overburden loads: insights from physical and numerical models. Tectonophysics 473(3):324–340

Scholtès L, Donzé FV (2015) A DEM analysis of step-path failure in jointed rock slopes. CR Mec 343(2):155–165

Sinha UN, Singh B (2000) Testing of rock joints filled with gouge using a triaxial apparatus. Int J Rock Mech Min Sci 37(6):963–981

Tang HM, Zou ZX, Xiong CR, Wu YP, Hu XL, Wang LQ, Lu S, Criss RE, Li CD (2015) An evolution model of large consequent bedding rockslides, with particular reference to the Jiweishan rockslide in Southwest China. Eng Geol 186:17–27

Toshikazu K (1981) An analysis of excavation in strain-softening rock mass. In: Proceedings of the Japan Society of civil engineers, pp 107–17

Troncone A (2005) Numerical analysis of a landslide in soils with strain-softening behaviour. Géotechnique 55(8):585–596

Wang GJ, Kong XY, Gu YL, Yang CH (2011) Research on slope stability analysis of super-high dumping site based on cellular automaton. Procedia Eng 12:248–253

Wang XB, Ma J, Liu LQ (2013) Numerical simulation of large shear strain drops during jog failure for echelon faults based on a heterogeneous and strain-softening model. Tectonophysics 608:667–684

Wu HM, Shu YM, Zhu JG (2011) Implementation and verification of interface constitutive model in FLAC 3D. Water Sci Eng 4(3):305–316

Xiumina L, Congxin C, Yun Z (2012) Optimum arrangement of prestressed cables in rock anchorage. Procedia Earth Planet Sci 5:76–82

XP (1997) Essai de Gonflement a l'oedometre. In P94-071-2

Xuegui S, Yanbin L, Yongkang Y (2011) A research into extra-thick compound mudstone roof roadway failure mechanism and security control. Procedia Eng 26:516–523

Zhang G, Zhang JM (2007) Simplified method of stability evaluation for strain-softening slopes. Mech Res Commun 34(5):444–450

Zhang K, Cao P, Bao R (2013) Progressive failure analysis of slope with strain-softening behaviour based on strength reduction method. J Zhejiang Univ Sci A 14(2):101–109

Zheng LN (2012) Research of failure mechanism and the local failure zones for consequent slope based on strain softening theory. Southwest Jiaotong University, Chengdu

Zhou AZ, Lu TH (2009) Elasto-plastic constitutive model of soil-structure interface in consideration of strain softening and dilation. Acta Mech Solida Sin 22(2):171–179